











Second-harmonic and linear spectroscopy of α -In₂Se₃Yujin Cho ¹, Sean M. Anderson ^{2,*}, Bernardo S. Mendoza ², Shun Okano ³, N. Arzate ², Anatoli I. Shkrebti ⁴, Di Wu, ¹ Keji Lai ¹, Ramón Carriles ², D. R. T. Zahn ³ and M. C. Downer ^{1,†}¹Department of Physics, University of Texas at Austin, Austin, Texas 78712, USA²Centro de Investigaciones en Óptica, León, Guanajuato 37150, México³Semiconductor Physics, Chemnitz University of Technology, 09107 Chemnitz, Germany⁴Ontario Tech University, Oshawa, Ontario, Canada L1G 0C5

(Received 12 October 2021; accepted 23 February 2022; published 15 March 2022)

We report spectroscopic measurements of optical transmission, ellipsometry, and second-harmonic generation (SHG) from as-grown vapor-deposited α -In₂Se₃ nanoflakes ranging in thickness from a single quintuple layer (QL) to bulk material. We compare these measurements with *ab initio* calculations of structural and optical properties. Linear optical measurements yield thickness-dependent band gaps and dielectric functions, while SHG diagnoses microscopic film structure and ferroelectric polarization. The rotational anisotropy of SHG for *s*-polarized incident photons of energy 1.4 eV reveals crystalline symmetry and orientation of individual QLs. Peak SHG intensity increases from one to three QLs, then decreases for larger numbers, tracking thickness-dependent trends in the second-order susceptibility components χ^{xxx} and χ^{zzx} . Comparison of measured and calculated SHG spectra for *s*-polarized photons of energies between 1.2 and 1.7 eV incident upon two QL samples discriminates among candidate stacking arrangements, and favors an arrangement with electric polarization vectors of the two QLs pointing outward in opposite directions.

DOI: [10.1103/PhysRevMaterials.6.034006](https://doi.org/10.1103/PhysRevMaterials.6.034006)

I. INTRODUCTION

Ultrathin III-VI semiconductors underlie a host of emerging nano-optoelectronic applications, including broadband detectors, solar cells, and phototransistors, because they combine large thickness-dependent band gaps with high carrier mobility [1,2]. In addition to bulk III-VI crystals, these materials form two-dimensional (2D) hexagonal nanofilms only a few atoms thick [3–5]. In particular, indium (In) and selenium (Se) can form several single-phase and layered In-Se compounds: InSe [6], In₂Se₃, In₃Se₄ [7,8], and In₄Se₃ [9–11]. Of these, a rich variety of applications for In₂Se₃ have emerged [1,3–5,12,13] because of its advantageous optoelectronic properties. First of all, α -In₂Se₃ has a thickness-dependent band gap [14] which enables tuning of its optical properties [15,16]. Second, the crystal structure is temperature tunable, noncentrosymmetric α -In₂Se₃ transforms into centrosymmetric β -In₂Se₃ at 475 K [17], enabling phase-change memory applications [18,19]. Finally, thin-film In₂Se₃ is a 2D ferroelectric with switchable out-of-plane polarization down to a few layers [20]. In-plane ferroelectricity has been demonstrated in various 2D materials such as MoS₂, SnTe, and phosphorene analogs [21–23], but out-of-plane ferroelectricity is relatively rare. This is because when film thickness shrinks below some critical value, typically a few nanometers,

strong depolarization fields tend to suppress ferroelectricity, as observed in, e.g., perovskite thin films [24,25]. Nevertheless, in some 2D ferroelectrics, misfit strain [26,27], and/or out-of-plane chemical bonding [22] at the substrate-film interface can counteract depolarization, enabling switchable polarization down to a few layers. In the case of In₂Se₃, this is desirable for applications [28] such as miniature, high-speed memory devices with low-power consumption [29–33].

The basic In₂Se₃ structural unit consists of five alternating Se and In atoms that form a so-called quintuple layer (QL), as shown in Fig. 1. QLs bond to each other by the van der Waals (vdW) force. Numerous QL stacking arrangements [20] with parallel and opposite dipole moments [15,31,34] are possible, as Fig. 1(b) illustrates for two QLs. The two most energetically stable layered structures belong to the α and β phases. Both are semiconducting with energy band gaps in the optical range. The α phase has the lowest total energy and belongs to the $R3m$ space group; in contrast, the β phase is less energetically stable and belongs to the $R\bar{3}m$ space group. α -In₂Se₃ possesses room-temperature out-of-plane ferroelectricity down to a few layers [31,34–37], which is expected to persist even down to a single QL [20]. However, the strong dipole moment favors formation of 2D domains with opposite dipole orientations, to reduce electrostatic energy. The potential barrier for changing the dipole orientation is around 0.07 eV [20]. A few volts of applied electric potential in the perpendicular direction can switch the dipole directions of the QL [31]. Moreover, the magnitude of the spontaneous polarization does not increase linearly with thickness; it is expected to peak at three QLs, and to decrease with additional layers [20]. Knowledge of how spontaneous polarization changes

*Co-corresponding author: anderss@wfu.edu; Present address: Information Systems, Wake Forest University, Winston-Salem, NC 27109, USA.

†Co-corresponding author: downer@physics.utexas.edu

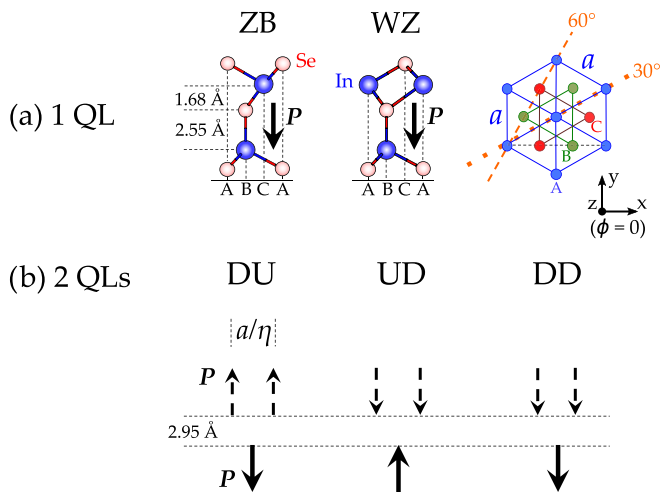


FIG. 1. Candidate α - In_2Se_3 atomic configurations for band structure and optical calculations. (a) Single-QL variants based on zincblende (ZB, left) and wurtzite (WZ, center) units arranged in $R3m$ -symmetry 2D crystal with lattice constant $a = 4.106 \text{ \AA}$ (right). (b) Three possible vertical configurations of electric polarization vectors \mathbf{P} in 2-QL samples, showing horizontal separation a/η [$\eta = \sqrt{3}(2)$ for 60° (30°)] of equivalent energy minima, resulting from translating one QL along the 60° (orange dashed) or 30° (orange dotted) trajectories shown in the right-hand diagram in (a). Here, $\eta = \sqrt{3}(2)$ denotes the factor by which the two energy minima of the top layer differ from a when it is translated along 60° (30°) directions. Thus, $|a/\eta| = 2.371 \text{ \AA}$ (2.053 \AA).

with thickness and microscopic atomic arrangement is crucial for engineering ultrathin α - In_2Se_3 devices down to single-QL dimensions.

The objective of this study is to connect systematic thickness-dependent trends in noninvasive linear and second-harmonic (SH) optical spectra of α - In_2Se_3 to thickness-dependent changes in microscopic structure. Linear transmission spectra straightforwardly yield the imaginary part of the dielectric function; spectroscopic ellipsometry yields full dielectric functions with high sensitivity, and corroborates transmission spectra. Together they characterize thickness-dependent electronic band structures. Optical second-harmonic generation (SHG), on the other hand, is sensitive to in-plane crystalline symmetry of individual QLs, and to built-in polarization. SHG characterizes ferroelectric properties because the net polarization breaks inversion symmetry, leading to a nonvanishing second-order nonlinear optical susceptibility $\chi^{(2)}$. SHG can thus identify promising ferroelectric behavior in candidate materials that for now can only be fabricated in device-incompatible form such as monolayer nanoflakes [34], or for which the chemistry of contacting electrodes that avoid leakage currents is not yet developed [33,38]. For similar reasons, both theoretical [5,16,39,40] and experimental [41–43] SHG studies have been carried out on other 2D materials. We present results of linear and SHG spectroscopic measurements along with *ab initio* calculations that relate the spectra to underlying structural and ferroelectric properties of few-layer α - In_2Se_3 .

The paper is organized as follows. In Sec. II, we describe experimental and computational methods. In Sec. III, we

present our measured and calculated spectra for both layered and bulk material. In Sec. IV, we discuss the relationships between optical properties and underlying thickness-dependent band structure of α - In_2Se_3 , and between SHG and ferroelectric polarization. Lastly, we state our conclusions in Sec. V.

II. METHODS

A. Samples

In_2Se_3 nanoflakes were grown on fluorophlogopite mica substrates by vapor phase deposition, which provides highly crystalline samples and well-controlled thickness profiles [15,34,44,45], as confirmed previously by transmission electron microscopy (TEM) [15]. The flakes were synthesized by vdW epitaxy in a 1-in. diameter horizontal quartz tube furnace (Lindberg Blue M HTF55667C). Bulk In_2Se_3 powder (99.99%, Alfa Aesar) was placed at the center and heated to 740°C . A steady flow of argon gas (20 Torr, 30–200 standard cubic centimeters per minute) carried the vapor toward one end of the tube, and deposited it on mica substrates, placed 7 to 12 cm away from the heated center, forming multi-QL In_2Se_3 flakes with distinct triangular shapes typically a few tens of microns wide – as well as single-QL flakes, which instead formed rounded shapes. After 10 min, the tube was cooled down to room temperature at a rate below $5^\circ\text{C}/\text{min}$. We confirmed the thickness of the layers to be 0.84 nm per QL using atomic force microscopy (see Supplemental Material [46]), consistent with the reported thickness measured with transmission electron microscopy [34]. The atomic positions of the QLs can be identified from TEM studies, although they cannot distinguish between the zincblende, wurtzite, or other structure [34,47,48].

The crystallinity was confirmed using rotational-anisotropic SHG (RA-SHG) microscopy, which verified the presence of the α phase of In_2Se_3 . There are three mirror lines or axes on the QL plane of the $R3m$ crystal class structure. Only one of these is unique and is along the horizontal axis; the other two are generated by in-plane 120° rotation along the threefold z axis. RA-SHG patterns demonstrate this mirror symmetry with six-lobe patterns. Similar patterns can also be observed in transition metal dichalcogenide (TMD) monolayers with hexagonal symmetry; for instance, strong SHG is observed in noncentrosymmetric single-monolayer MoS_2 , that also has threefold rotational symmetry [49].

B. Optical measurements

Spectroscopic ellipsometry (SE) on the bulk material was performed on a microimaging ellipsometer Nanofilm EP4 (Accurion GmbH), equipped with a xenon arc lamp with a wavelength range from 950 to 250 nm (photon energy 1.3 to 4.96 eV, respectively). A single diffraction grating produced monochromatic incident light, which impinged on the samples at various oblique angles to the surface normal. Lack of a reflected signal from an underlying substrate and of surface oxide layers simplified analysis of ellipsometric data, enabling us to use the Fresnel equations [50]

$$\langle\langle n \rangle\rangle + i\langle\langle k \rangle\rangle = \sin^2 \theta \left[1 + \tan^2 \theta \left(\frac{1 - \rho}{1 + \rho} \right)^2 \right]$$

to convert measured Ψ and Δ directly into refractive index n and extinction coefficient k . Here, $\rho = \tan \Psi e^{i\Delta}$ is the complex ratio of p to s field components after reflection, Δ is the phase shift, and θ is the angle of incidence. We estimated the optical band gap for the bulk material from the photon energy at which k vanishes.

Optical transmission spectroscopy was performed on 1 through 12, 25, and 37 QL samples using the same equipment at normal incidence. The transmitted light was collected and imaged with $\sim 1 \mu\text{m}$ spatial resolution to a detector array with a Nikon 50 \times long working distance microscope objective (N.A. = 0.45), enabling signals from within the boundaries of a single tens-of-micron-sized flake to be analyzed. Reflection from these samples was negligible, facilitating conversion of transmission to absorption spectra using the Beer-Lambert law. We obtained band gaps by creating Tauc plots [51,52] from the absorption spectra, and linearly extrapolating the absorption edge [14]. See the Supplemental Material for more procedural details [46].

For SHG, 140-fs pulses at 80 MHz repetition rate from a Ti:sapphire laser (Coherent Chameleon Vision II) were focused onto samples at 45 $^\circ$ from the surface normal to spot size (FWHM) 3 μm . A $\lambda/2$ -wave-plate controlled incident beam polarization, which we label with lowercase s (or p) to denote electric field perpendicular (or parallel) to the plane of incidence. Here we report results obtained entirely with s -polarized incident light. A photon-counting photomultiplier tube detected reflected second-harmonic (SH) light through a bandpass filter and polarization analyzer, which selected S or P , which we denote by capital letters when referring to SH light. We optimized focal plane position by dithering sample position along the surface normal during data acquisition until SHG intensity was optimized. For extended measurements involving sample translation and rotation or laser tuning, we kept average laser power below 2 mW (i.e., 25 nJ/pulse) to avoid laser-induced charging [53] or sample damage. However, power could be increased momentarily to enhance weak SHG signals, e.g., from single QLs.

To probe crystal symmetry, we measured normalized, rotational-anisotropic (RA) S - or P -polarized SHG intensity as a function of azimuth ϕ at fixed reference photon energy (wavelength) 1.59 eV (780 nm), with the laser pulse focus fixed within a region of known thickness. To identify such regions, we obtained SHG micrographs of individual nanoflakes by rastering the sample in 2- μm steps along the surface plane over a 300 $\mu\text{m} \times 300 \mu\text{m}$ area bracketing the nanoflake under study, while monitoring SHG at an RA-SHG peak in a fixed polarization configuration. Regions ranging in thickness from 1 to 5 QLs were easily identified in such micrographs via their characteristic triangular shapes and abrupt increments in SHG intensity at their boundaries.

For spectroscopic SHG, we fixed ϕ at an RA-SHG peak for each polarization configuration (sS and sP), and the laser focus within a uniformly thick region, then tuned photon energy (wavelength) from 1.19 eV (1040 nm) to 1.70 eV (730 nm). All measurements were checked for consistency by collecting data from several regions on the same sample, as well as from different flakes with the same number of QLs. In addition, all spectroscopic SHG data were normalized to reference SHG that a split-off, equivalently-focused portion of the incident

beam produced in a spectrally flat z -cut quartz wedge, to correct for variations in intensity and pulse structure during laser tuning. Measurements using a single reference wavelength with the incident plane at an RA-SHG peak were used to determine relative SHG intensity between different sample thicknesses and polarization configurations.

C. Computational methods

The QLs for our calculations were based on either zincblende (ZB) or wurtzite (WZ) structural units with atomic layers sequenced vertically in the order Se-In-Se-In-Se [see Fig. 1(a), left and center], but with top-layer Se atoms shifted laterally from pure ZB or WZ lattice positions to form energetically stable ground-state structures [20]. Atoms in each atomic layer of a QL form a triangular lattice with in-plane lattice constant $a = 4.106 \text{ \AA}$ [Fig. 1(a), right] and $R3m$ space-group symmetry, the same symmetry as bulk $\alpha\text{-In}_2\text{Se}_3$, in agreement with previous calculations [20]. ZB- and WZ-based QLs are stable at room temperature and are nearly energetically degenerate, with a total-energy difference below 0.005 eV/QL [20]. Each Se atom in the central layer bonds vertically to a single In atom in one neighboring layer, but obliquely to three In atoms in the opposite neighboring layer, resulting in dissimilar Se-In interlayer spacings of 2.55 and 1.68 \AA , respectively [Fig. 1(a), left]. This broken centrosymmetry underlies both spontaneous out-of-plane electric polarization \mathbf{P} and second-order nonlinear optical susceptibility $\chi^{(2)}$ in both variants of the single QL.

To determine candidate structures for 2 QLs, we calculated total energy while translating one QL over the other along each of two horizontal basis vectors, labeled “60 $^\circ$ ” and “30 $^\circ$ ” in Fig. 1(a), right. Each translation yielded two equivalent energy minima separated by a/η , where $\eta = \sqrt{3}$ (2) for 60 $^\circ$ (30 $^\circ$). The 2-QL structure at the 60 $^\circ$ energy minima retained overall $R3m$ symmetry, for which only four components of the second-order nonlinear susceptibility tensor $\chi^{(2)}$ are nonzero and independent:

$$\begin{aligned} -\chi^{xxx} &= \chi^{xyy} = \chi^{yxy}, & \chi^{xxz} &= \chi^{yyz}, \\ \chi^{zxx} &= \chi^{zyy}, & \chi^{zzz} &. \end{aligned}$$

The corresponding structure at the 30 $^\circ$ energy minima, on the other hand, possessed lower symmetry, resulting in additional nonzero $\chi^{(2)}$ components (xzz , xyx , yxx , yyy , yzx , zyx , zxx). Single-wavelength RA-SHG measurements can distinguish these symmetries, and thus narrow the allowable range of 2-QL stacking arrangements significantly. Associated with the 60 $^\circ$ and 30 $^\circ$ horizontal energy minima were three possible vertical configurations of the two single-QL \mathbf{P} vectors, shown in Fig. 1(b): down-up (DU), up-down (UD), and down-down (DD). Energy minimization calculations [54] with respect to the vertical translation yielded an inter-QL separation of $\sim 2.95 \text{ \AA}$ for both ZB and WZ, independent of horizontal translation or dipole stacking, with energy difference less than 0.014 eV throughout this range, and consistent with prior quantum molecular dynamics calculations [19]. We therefore fixed the inter-QL separation at 2.95 \AA throughout this work. Thus, after energy minimization, we are left with two horizontal and three vertical (\mathbf{P}) configurations for both ZB and WZ, for a total of 12 candidate 2-QL structures.

We carried out G_0W_0 [55] calculations at the Γ point to obtain self-corrected band gap values for 1 QL, 2 QLs, and bulk using the ABINIT code [56–58] with Troullier-Martins pseudopotentials [59]. These values were then used to adjust eigenenergies via a rigid scissors shift for all spectroscopic calculations. We calculated the dielectric function for bulk α - In_2Se_3 within the time-dependent density functional theory (TDDFT) framework using the DP [60,61] code, where the independent-particle response function was constructed using Kohn-Sham orbitals, within the random phase approximation including local-field effects.

For 1 QL (ZB and WZ) and each of the 12 candidate 2-QL configurations, we calculated band structure, dielectric functions $\epsilon(\omega)$ [62], and all components of $\chi^{(2)}$ using the TINIBA code [63] within the independent-particle density functional theory local density approximation (DFT-LDA) framework [64], and normalized to the supercell vacuum region [65]. *Ab initio* $\chi^{(2)}$ calculations for higher QL numbers were prohibitively expensive. The application of the Coulomb cutoff to the electronic screening, and the large supercell volumes required to eliminate spurious interactions between adjacent slabs vastly increases the numerical burden for these types of materials. For comparison with measured SHG spectra, we calculated SHG radiation yield, defined by

$$\mathcal{R}_i(\omega) \equiv I_i(2\omega)/I^2(\omega) \quad [i = sS, sP, pS \text{ or } pP], \quad (1)$$

from the $\chi^{(2)}$ tensor components and polarization-dependent Fresnel factors using the SHGYIELD PYTHON package [66], taking into account optical properties of all three layers of the sample (air, In_2Se_3 film, and mica substrate) and the thickness of the In_2Se_3 films [67,68]. In Eq. (1), $I(\omega)$ and $I_i(2\omega)$ denote fundamental and SH light intensity, respectively, at the sample, and the subscript i denotes the polarization configuration. We limited this study to sS and sP because they involve a minimum number of $\chi^{(2)}$ components, simplifying theory-experiment comparison. For example, for $R3m$ symmetry R_{sS} depends only on χ^{xxx} , eliminating the need to consider phase differences between different $\chi^{(2)}$ components; likewise, \mathcal{R}_{sP} depends only on χ^{xxx} and χ^{zxz} .

Our computational procedure tends to yield spectral features that are redshifted from their actual values by 0.1 to 0.2 eV. The most important reason for this is our use of the G_0W_0 gap, which slightly underestimates the actual gap, for the scissors shift. In addition, our use of the independent-particle approximation excludes excitonic effects, which can further upshift SHG spectra [39]. Although the assumption of temperature $T = 0$ introduces a slight compensating blueshift of calculated spectra from spectra measured at room temperature [69,70], the redshift dominates, and must be anticipated when comparing calculated with experimental SHG spectra. See Supplemental Material for more details on the calculations and structural analysis [46].

III. RESULTS

A. Linear optical results

1. Optical images

Figures 2(a) and 2(b) show white-light optical images of two α - In_2Se_3 flakes. More absorptive thicker regions show

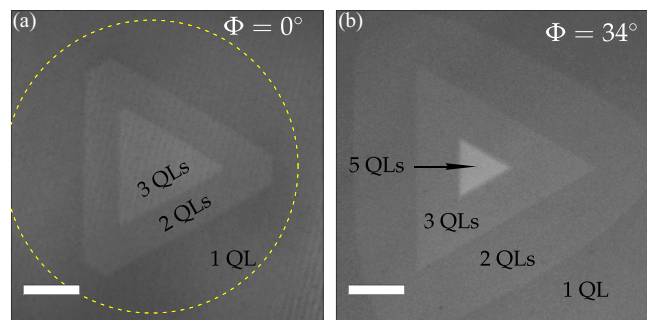


FIG. 2. White-light microscopic optical images from few-QL α - In_2Se_3 . Image for (a) $\Phi = 0^\circ$ and (b) 34° samples. Yellow dotted line in (a) shows approximate edge of 1-QL sample.

the best contrast [e.g., 5-QL center triangle in Fig. 2(b)], while 1-QL regions are barely visible (reflectivity $\sim 6\%$ above background). For the flake in Fig. 2(a) (hereafter the $\Phi = 0^\circ$ sample), all QLs are oriented along the same direction. For the flake in Fig. 2(b) (hereafter the $\Phi = 34^\circ$ sample), the bottom QL is rotated 34° with respect to overlying QLs.

2. Optical transmission spectra

Figure 3(a) presents measured transmission spectra for 1–5, 7, 12, 25, and > 37 QL samples over an energy range 1.5 to 3.7 eV. At each photon energy, total sample transmission was divided by that of the bare mica substrate, to isolate the optical response of the nanoflake. Shaded regions represent

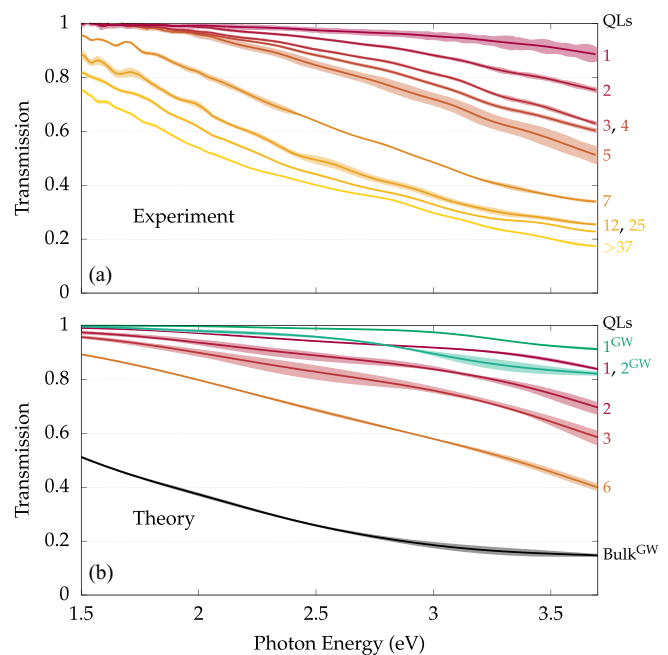


FIG. 3. Measured and calculated linear optical response: (a) experimental transmission spectra for layered α - In_2Se_3 in the range of 1.5 to 4 eV, for 1 to > 37 QLs; (b) theoretical results for 1–3 QLs, 6 QLs, and bulk. Shaded regions around the experimental (theoretical) results represent measurement uncertainty (stacking variations) for any given number of QLs. Theoretical results have a Gaussian broadening of $\sigma = 0.30$ eV.

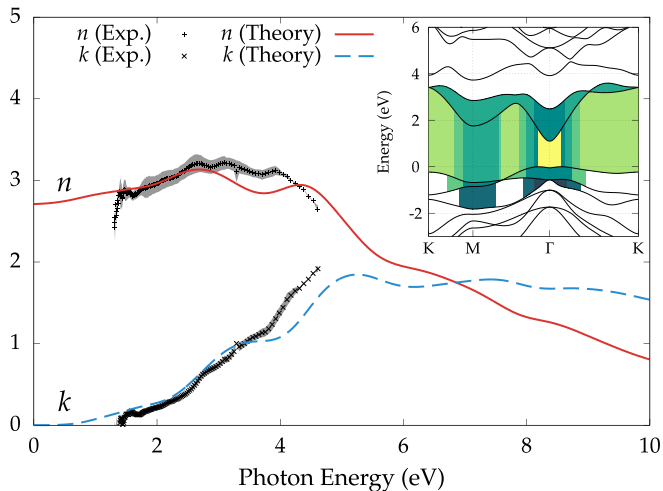


FIG. 4. Real (n) and imaginary (k) parts of the complex index of refraction for bulk α - In_2Se_3 , calculated over photon energy range 0 to 10 eV (red and dashed blue curves) and measured from 1.5 to 5 eV (black '+'s and 'x's). Theoretical curves use G_0W_0 quasiparticle correction for the band gap of 1.11 eV. Inset: band structure along $\text{K} \rightarrow \text{M} \rightarrow \Gamma \rightarrow \text{K}$ points in the Brillouin zone. Theoretical results have a Gaussian broadening of $\sigma = 0.30$ eV.

the standard deviation of measurements taken from different spots on the same flake.

Figure 3(b) presents calculated transmission spectra for 1–3 QLs, 6 QLs, and bulk. Here, shaded regions represent the range of values calculated for the candidate stacking arrangements while solid curves represent the average value for each QL number. As mentioned above, we considered 12 arrangements for 2 QLs; we also ran select arrangements (selected at random) for 3 QLs (8 variations), 6 QLs (2 variations), and bulk (8 variations). The narrowness of the shaded regions demonstrates the insensitivity of optical transmission to stacking arrangement. For results without G_0W_0 correction, the discrepancy with experiment is $\sim 7\%$. For the 1- and 2-QL results with this correction (labeled with “GW” superscript), agreement is better than 2% and 4%, respectively, across the entire range. Overall, our calculations correctly represent the decreasing transmission observed from 1.5 to 3.7 eV, and are consistent with previous experimental [14] and theoretical [13,16] results.

3. Spectroscopic ellipsometry

Figure 4 compares experimental (1.5 to 5 eV) complex refractive index spectra from SE with theoretical (0 to 10 eV) spectra from TDDFT calculations for bulk α - In_2Se_3 . Since calculated results for wurtzite and zincblende bulk structures were nearly identical, Fig. 4 presents an average of the two. Theoretical spectra include a quasiparticle correction of 0.66 eV, obtained from an *ab initio* G_0W_0 calculation, placing the bulk optical band gap (at the Γ point) at 1.11 eV. This value is 7.5% below the measured value (1.2 eV), and slightly below previously reported G_0W_0 -corrected optical band gap values [14]. The measured $n(k)$ differ by less than 15% (30%) from calculated values throughout the measured photon energy range. The yellow region in the calculated band structure

TABLE I. Measured and calculated optical band gaps for layered and bulk α - In_2Se_3 . Measured values were obtained from Tauc plots based on transmission data [Fig. 3(a)], theoretical values from *ab initio* G_0W_0 calculations at the Γ point.

Sample	Experiment (eV)	G_0W_0 (eV)
1 QL	2.344 ± 0.232	2.241
2 QLs	2.123 ± 0.075	1.820
3 QLs	1.987 ± 0.014	
4 QLs	1.960 ± 0.010	
5 QLs	1.963 ± 0.013	
Bulk	1.167	1.110

(Fig. 4, inset) highlights optical transitions around the Γ point, which comprise the optical band gap. Darkening shades of green represent transitions from increasingly separated band pairs. The greatest density of transitions occurs above 3.0 eV. Transitions originating on the highest, second-highest, and third-highest valence bands and terminating on the two lowest conduction bands are enough to describe the important features of the optical spectra.

4. Optical band gaps

The middle column of Table I and black circles in Fig. 5 present optical band gaps for 1–5 QLs and for bulk α - In_2Se_3 . Error bars represent the standard deviation of an ensemble of Tauc plot fittings allowed by the uncertainty of near-band-edge transmission. The right column in Table I and red squares in Fig. 5 show calculated gaps at the Γ point for 1–2 QLs and bulk. Band gaps decrease steadily from ~ 2.3 eV for 1 QL down to 1.17 eV for bulk. The bulk value is consistent with reported experimental [5,14,19,47,48,71–79] and theoretical [5,16,20,72] band gaps for α - In_2Se_3 . Our G_0W_0 bulk gap (1.11 eV) is within 5% of our measured bulk gap, while our G_0W_0 1 QL (2 QL) gap is within 5% (15%) of the measured gap. The calculated band gap for 2 QLs varied by less than 2% among the 12 candidate stacking configurations, and thus provided no basis for distinguishing among them. A simple 1D quantum confinement model, in which band gap varies inversely with squared film thickness [14], accounts for the band gap variations shown in Table I and Fig. 5. Gap

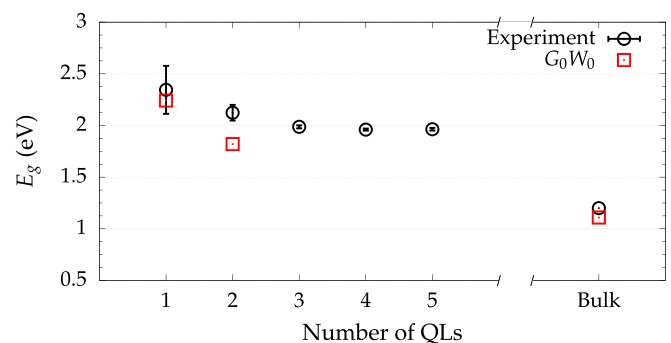


FIG. 5. Band gap values obtained from optical transmission measurements (black circles), and from G_0W_0 calculations (red squares). All theoretical values were calculated at the Γ point.

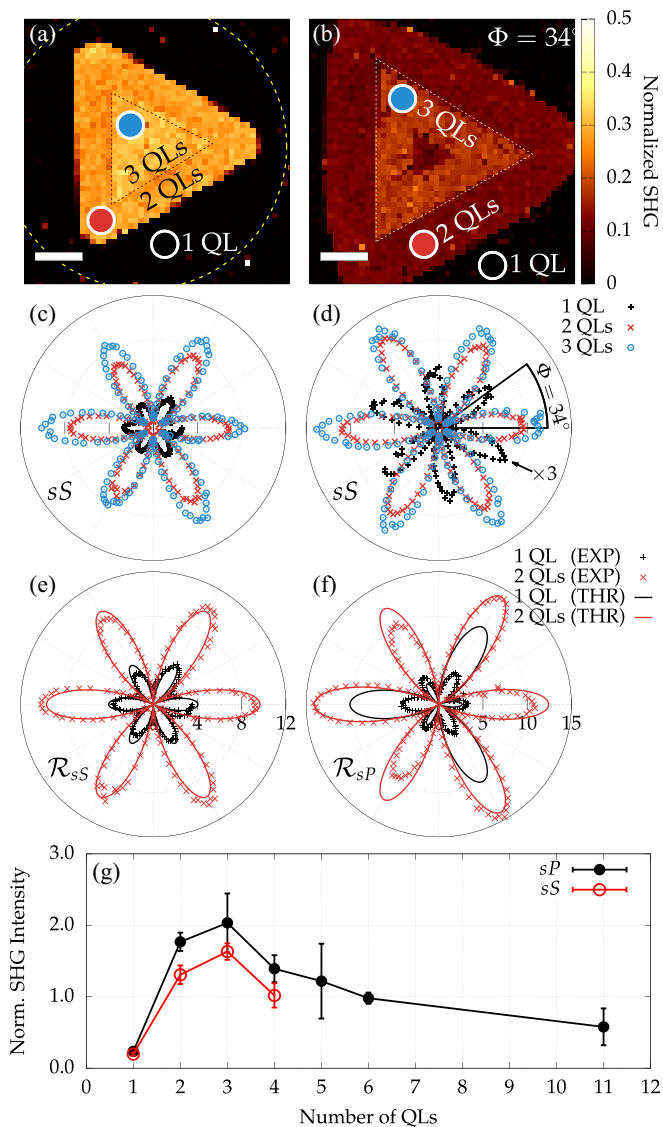


FIG. 6. SHG images and data at 1.59 eV (780 nm) from few-QL α - In_2Se_3 . (a), (b) Scanning SHG micrographs with sS polarization of $\Phi = 0^\circ$ (a) and 34° (b) samples. Yellow dotted line in (a) shows approximate edge of 1 QL sample. Number of QLs is labeled in each region. Angle Φ : crystallographic rotation of second from first QL; white bars: $50 \mu\text{m}$. (c)–(f) RA-SHG patterns for 1 (black +’s), 2 (red \times ’s) or 3 (blue circles) QLs; (c) sS polarization for $\Phi = 0^\circ$ and (d) 34° ; (e) \mathcal{R}_{sS} and (f) \mathcal{R}_{sP} for $\Phi = 0^\circ$; units for theoretical curves (e), (f) are $10^{-22} \text{cm}^2/\text{W}$. (g) SHG intensity (normalized to SHG from α -quartz) vs number of QLs for sP (black filled circles) and sS (open red circles) polarization configurations, $\Phi = 0^\circ$.

narrowing with increasing thickness also emerges from our first-principle calculations [80].

B. SHG results

1. SHG micrographs

Figures 6(a) and 6(b) show scanning SHG micrographs taken with sS polarization at photon energy (wavelength) 1.59 eV (780 nm) for the $\Phi = 0^\circ$ and $\Phi = 34^\circ$ samples in Figs. 2(a) and 2(b), respectively. Since the mica substrate is

centrosymmetric, strong SHG occurs only within the noncentrosymmetric α - In_2Se_3 nanoflakes, resulting in strong contrast between sample and substrate. SHG signals $\sim 15\times$ above background SHG signals were obtained from 1 QL, far exceeding the contrast achievable with linear optical imaging.

2. Rotational-anisotropic single-wavelength SHG

Figures 6(c) and 6(d) show polar plots of SHG intensity vs sample azimuthal rotation angle ϕ , using sS polarization with incident photons of energy 1.59 eV (780 nm) focused on 1-QL (black crosses), 2-QL (red \times ’s), or 3-QL (blue circles) regions indicated by colored circles in Figs. 6(a) and 6(b). In Fig. 6(c), SHG maxima from all three regions are aligned in the same direction, indicating three commonly aligned QLs. The same was observed for most of the 15 other nanoflakes studied. Figure 6(d) shows a rare exception, where the maxima from the 1-QL region are rotated $\Phi = 34^\circ$ from the maxima of the 2-QL and 3-QL regions, indicating a corresponding rotation of the bottom QL with respect to the top two.

The commonly oriented polar patterns in Fig. 6(c) provide evidence that most 1-, 2-, and 3-QL samples share a common $R3m$ symmetry. For this symmetry, the SHG yield for sS polarization takes the simple form [67,68]

$$\mathcal{R}_{sS}(2\omega, \phi) = |A(\omega) \sin 3\phi|^2, \quad (2)$$

where $A(\omega) = F(\omega)F(2\omega)\chi^{xxx}$, $F(\omega)$, and $F(2\omega)$ are Fresnel factors. ϕ is the azimuthal angle with respect to the x axis; $\phi = 0$ corresponds to the plane of incidence along the horizontal direction in Fig. 1(a). A lower 2-QL symmetry, e.g., due to a 30° translation of layer 2 with respect to layer 1 as shown in Fig. 1(a) (right), would have led to a more complicated polar pattern for 2 QLs. Observation of simple six-lobed patterns enables us to rule out the 30° translation option, thereby reducing the number of candidate structures for 2 QL spectroscopic SHG calculations from 12 to 6. Figures 6(e) and 6(f) compare results between experiment and theory for 1 QL and 2 QLs for sS and sP polarizations. The theoretical QL structures used here were wurtzite, with 2 QLs in an outward-facing dipole orientation. \mathcal{R}_{sS} shows close agreement between experiment and theory, with an overall lobe intensity ratio difference of 15% across the entire range of angles. On the other hand, some of the lobes of \mathcal{R}_{sP} from 1 QL are disproportionate in size, and do not maintain the correct intensity ratio between 1 QL and 2 QLs. There is a 45% difference between the experimental and calculated intensity ratio of the smaller lobes, and an 80% difference for the larger lobes.

Lastly, Fig. 6(g) shows the scaling of SHG signal strength with thickness. SHG intensity increases nearly 10-fold from 1 to 2 QLs, then an additional 25% from 2 to 3 QLs. SHG from 5 QLs [Figs. 2(b) and 6(b), small center triangle] is 40% weaker than from the surrounding 3 QL region.

3. SHG spectra

Figure 7 presents spectra of SHG intensity normalized to SHG from α -quartz for sP [Figs. 7(a) and 7(c)] and sS [Figs. 7(b) and 7(d)] polarization configurations for $\Phi = 0^\circ$ (top row) and 34° (bottom row) samples of 1- to 4-QL thickness. Data for 1 QL for $\Phi = 0^\circ$ [top panels 7(a) and 7(b)]

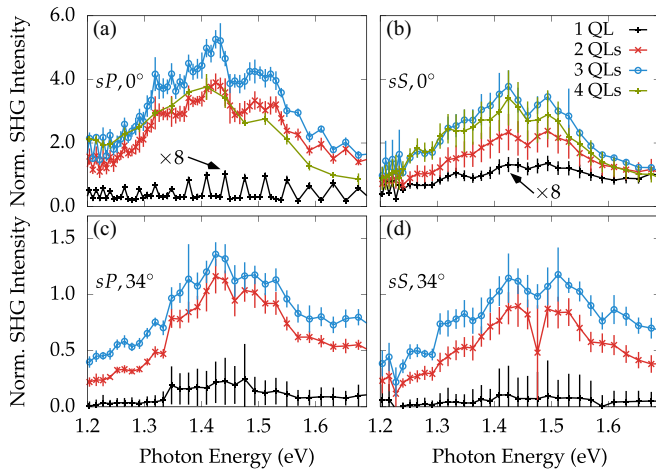


FIG. 7. SHG spectral intensity for 1–4 QL samples of $\Phi = 0$ [top row: (a) sP , (b) sS polarization], and $\Phi = 34^\circ$ [bottom row: (c) sP , (d) sS] α - In_2Se_3 , normalized to near-spectrally-flat SHG intensity from α -quartz. Data for 1 QL (black) for $\Phi = 0$ [top panels (a) and (b)] has been multiplied $\times 8$ for visibility.

have been multiplied $\times 8$ for ease of visualization. All 2–4 QL spectra exhibit a broad resonance centered near 1.4 eV, but SHG is several times stronger from $\Phi = 0^\circ$ than from $\Phi = 34^\circ$ samples. For $\Phi = 0$, sP SHG is $\sim 50\%$ stronger than for sS polarization.

Figure 8 plots calculated SHG radiation yield spectra \mathcal{R}_{sP} (top row) and \mathcal{R}_{sS} (bottom row) for the six candidate 2-QL configurations ($\Phi = 0^\circ$) that are consistent with $R3m$ symmetry: wurtzite (left column) and zincblende (right column)

structural units; DU (solid red), UD (dashed blue), and DD (dotted-dashed green) stacking configurations, along with the calculated 1-QL spectra (black solid curves) for both wurtzite and zincblende units. Measured \mathcal{R}_{sP} (top row) and \mathcal{R}_{sS} (bottom row) for 1 (black + with error bars) and 2 QLs (red \times with error bars), identical to curves in Figs. 7(a) and 7(b) are shown for comparison. In contrast to calculated linear optical spectra for 2 QLs, the calculated $\mathcal{R}_{sP,sS}$ shown in Fig. 8 vary widely in spectral shape, amplitude, and polarization dependence among the candidate structures. Comparison of calculated with measured SHG spectra thus provide a basis for choosing among them.

The wurtzite DU configuration [Figs. 8(a) and 8(c), solid red curves] yields the best agreement with data, in three respects. First, the spectral shape of the calculated $\mathcal{R}_{sP,sS}$ curves in the $1.0 < \hbar\omega < 1.55$ eV window match corresponding data in the $1.15 < \hbar\omega < 1.7$ eV window well, and are redshifted by ~ 0.2 eV from them, as anticipated from our use of G_0W_0 band gaps with a rigid scissors shift approach for the components of $\chi^{(2)}$ (see Sec. II C). Second, this calculation correctly reproduces the unaltered spectral shape and modest $\sim 50\%$ amplitude decrease from sP to sS polarization that is observed. Third, the several-fold stronger calculated SHG response from 2 QLs compared to 1 QL [Figs. 8(a) and 8(b), solid black curves] matches the observed experimental contrast.

Remaining calculated $\mathcal{R}_{sP,sS}$ curves match the data more poorly in one or more of these respects. The calculated $\mathcal{R}_{sP,sS}$ for the zincblende DU configuration [Figs. 8(b) and 8(d), solid red curves], though also consistent with the observed peak position and polarization dependence, yield a narrower

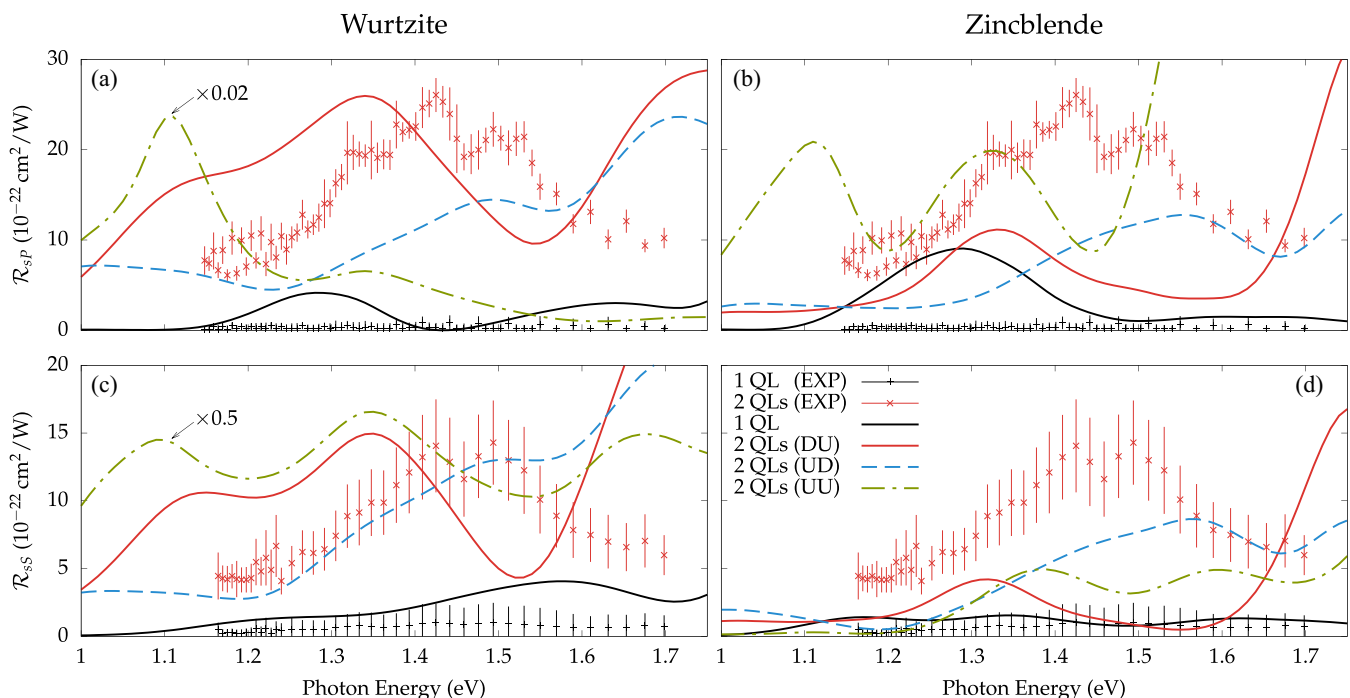


FIG. 8. Calculated SHG radiation yield spectra \mathcal{R}_{sP} (a), (b) and \mathcal{R}_{sS} (c), (d) for wurtzite (left column) and zincblende (right column) structural units for 2 QLs with DU (solid red), UD (dashed blue), and DD (dotted-dashed green) configurations. Calculated spectra for 1 QL (solid black), and measured spectra for 1 and 2 QLs (black + and red \times) are shown for comparison. Each calculated component of $\chi^{(2)}$ that is included in the SHG yield has a Gaussian broadening of $\sigma = 0.05$ eV.

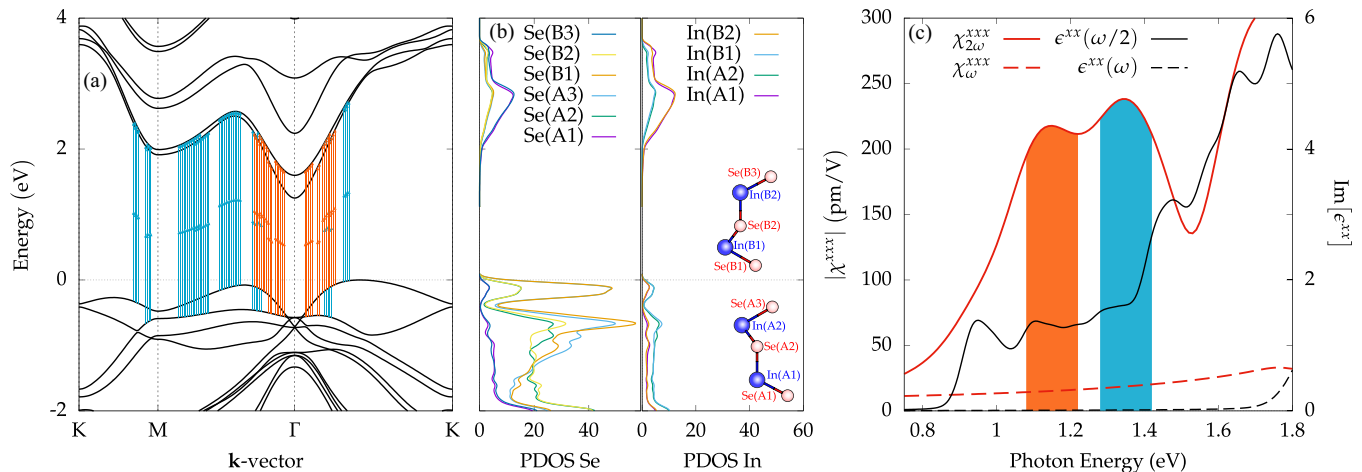


FIG. 9. Calculations for 2 QLs: (a) band structure (black curves), with two groups of two-photon transitions centered at fundamental photon energy 1.15 eV (orange) and 1.35 eV (blue) superimposed; (b) corresponding projected density of states (PDOS) for each atom in the 2-QL unit cell; (c) χ^{xxx} spectra (red), decomposed into ω (χ_{ω}^{xxx} , dashed), and 2ω ($\chi_{2\omega}^{xxx}$, solid) contributions, and $\text{Im}[\epsilon^{xx}]$ spectra (black), evaluated at ω (dashed) and 2ω (solid). All spectra are broadened with Gaussian width $\sigma = 0.05$ eV.

spectral peak than observed. Calculations for the UD configuration (dashed blue curves) yield a spectral peak that is blueshifted, rather than redshifted, from the observed peak. Finally, calculations for the DD configuration (dotted-dashed green) predict a much stronger polarization dependence in both spectral shape and amplitude than observed. Thus, analysis of SHG spectra strongly supports the DU stacking configuration for 2 QLs, with preference for the wurtzite structural unit.

IV. DISCUSSION

The calculated “best choice” SHG radiation yield spectra \mathcal{R}_{sP} and \mathcal{R}_{sS} in Figs. 8(a) and 8(c) (solid red curves) are related to the underlying band structure, linear dielectric function $\epsilon(\omega)$, and second-order susceptibility components χ^{xxx} , χ^{zxx} of the 2-QL layer with wurtzite DU structure. Figure 9(a) presents the band structure for this 2-QL configuration along the high-symmetry $K \rightarrow M \rightarrow \Gamma \rightarrow K$ points in the Brillouin zone. Vertical orange and blue arrows show concentrations of direct two-photon transitions at energies 2.3 and 2.7 eV, respectively, between the two highest (strongly split) valence bands and the two lowest (nearly degenerate) conduction bands. The highest projected density of states (PDOS) within the two-photon energy range probed by our SHG measurements occurs at these two energies, as can be seen in Fig. 9(b). Moreover, the inner selenium atoms Se(A2), Se(A3), Se(B1), and Se(B2) dominate the two-photon transitions, with a smaller contribution from the inner indium atoms In(A2) and In(B1). The PDOS for all of the atoms is dominated by p states with a less than 5% contribution from d states, and negligible contribution from f states. Consequently, two peaks in $|\chi_{2\omega}^{xxx}|$, plotted as a solid red curve in Fig. 9(c), and highlighted by red and blue regions beneath it, appear at these two-photon transition energies. They mirror peaks at the same energies in the calculated \mathcal{R}_{sP} and \mathcal{R}_{sS} in Figs. 8(a) and 8(c) (solid red curves). On the other hand, no peaks occur at the corresponding one-photon transitions (1.15 and 1.35 eV), as the featureless plot of $|\chi_{\omega}^{xxx}|$ [dashed

red curve, Fig. 9(c)] shows. Thus, the main peak observed in the SHG spectra [Figs. 7(a), 7(b), 8(a), and 8(c)] consists of two neighboring peaks, each comprised purely of two-photon transitions.

Black curves in Fig. 9(c) show the imaginary part of the in-plane component $\text{Im}[\epsilon^{xx}]$ of the dielectric function evaluated at ω (dashed) and 2ω (solid). $\text{Im}[\epsilon^{xx}(\omega)]$ enters into Fresnel factors which, together with χ^{xxx} and χ^{zxx} , determine SHG radiation yields \mathcal{R}_{sP} and \mathcal{R}_{sS} . $\text{Im}[\epsilon^{xx}(\omega)]$ begins to rise, signifying onset of absorption, at $\hbar\omega \approx 1.8$ eV, i.e., at the G_0W_0 optical band gap at Γ for 2 QLs (see Table I). Peaks in $\text{Im}[\epsilon^{xx}(\omega/2)]$ (solid black curve) due to one-photon interband transitions at 2.3 and 2.7 eV are evident, but much less prominent, than the corresponding two-photon peaks at these energies in $|\chi_{2\omega}^{xxx}|$. Moreover, a band-edge peak at 0.9 eV with no counterpart in the $|\chi_{2\omega}^{xxx}|$ spectrum appears. These differences in oscillator strength are attributable to dipole selection rules near high-symmetry points such as Γ that favor either odd-parity one-photon or even-parity two-photon transitions while suppressing the other [81]. Thus, although $\text{Im}[\epsilon^{xx}(\omega/2)]$ and $\chi_{2\omega}^{xxx}$ share some common spectral features, they differ markedly in overall spectral shape.

An important motivation behind SHG studies of thin-film ferroelectrics, stated in the Introduction, is to probe the net built-in polarization \mathbf{P} , which breaks inversion symmetry, and contributes to $\chi^{(2)}$. Yet the intuitive relationship between \mathbf{P} and $\chi^{(2)}$ is not transparent from results presented so far. Specifically, our calculations show that 1 QL has a nonzero out-of-plane polarization component P_z , whereas the P_z 's of the two QLs comprising the wurtzite DU structure point in opposite directions, and thus tend to cancel. Nevertheless, \mathcal{R}_{sP} and \mathcal{R}_{sS} are nearly $10\times$ stronger for 2 QLs than for 1 QL (see Fig. 7). Moreover, the macroscopic electric polarization that takes place on the medium under incidence of the optical field is directly related to the nonlinear susceptibility $\chi^{(2)}$, whose electronic origin in turn comes from interband two- and one-photon transitions, as shown in Fig. 9. For instance, in Fig. 9(c), we show $\chi_{2\omega}^{xxx}$ and χ_{ω}^{xxx} spectra corresponding to two- and one-photon contributions, respectively. Overall,

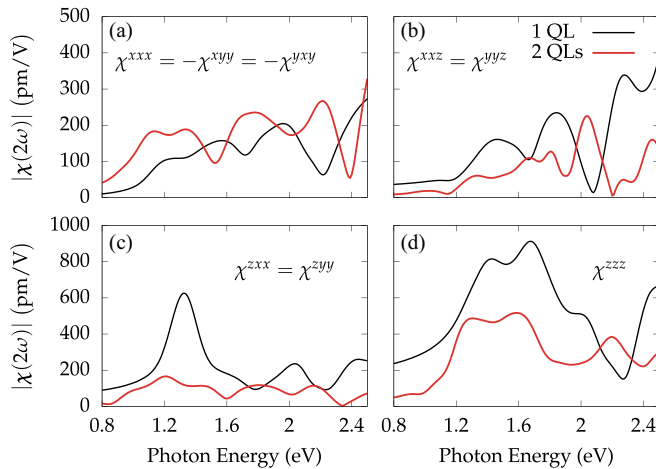


FIG. 10. Calculated spectra of the four independent components of $\chi^{(2)}$ for 1 QL (black) and 2 QLs (red) (a)–(d). Each includes a rigid scissors correction of 1.24 eV (1 QL) or 1.01 eV (2 QLs), yielding G_0W_0 band gaps (at the Γ point) of 2.24 eV for 1 QL and 1.82 eV for 2 QLs. All curves shown in (a)–(d) are broadened with a Gaussian of $\sigma = 0.05$ eV.

we see that $\chi_{2\omega}^{xxx}$ is larger than χ_{ω}^{xxx} . The orange and blue regions are shown to indicate that peak structures at 1.15 and 1.35 eV have contributions coming mainly from two-photon transitions. As shown in Fig. 9(a), in the former case, such transitions take place around the Γ point; while, in the latter case, most of the transitions occur along the M - Γ wave-vector path with a few of them taking place closer to the M and Γ points along the K - M and the Γ - K paths.

To see the connection between \mathbf{P} and $\chi^{(2)}$ transparently, we must consider calculated spectra of all four independent, nonzero $\chi^{(2)}$ tensor components for both 1 QL and the wurtzite DU 2-QL structure, plotted in Figs. 10(a)–10(d). Of these, χ^{zzz} is most directly connected, and thus most sensitive, to centrosymmetry breaking along the z axis, e.g., from P_z , and also has the largest amplitude [5,16]. We see from Fig. 10(d) that the amplitude $|\chi^{zzz}|$ for 1 QL is approximately $2 \times$ larger than for 2 QLs through most of the spectral range shown. This mirrors the intuitive picture of uncompensated P_z for 1 QL and canceling P_z 's for 2 QLs. χ^{zzz} , however, contributes only to \mathcal{R}_{pp} , and thus does not impress this simple relationship to P_z on SHG intensity in the \mathcal{R}_{sp} and \mathcal{R}_{ss} configurations considered here. This does not necessarily imply that \mathcal{R}_{pp} will mirror the intuitive dependence on P_z as clearly as χ^{zzz} . This will depend on the Fresnel factors and relative phases of χ^{xxz} [Fig. 10(b)] and χ^{zxx} [Fig. 10(c)], which also contribute to \mathcal{R}_{pp} . For the latter two components, the 1-QL/2-QL amplitude ratio is smaller and more frequency dependent than for χ^{zzz} . This example illustrates that observation of stronger SHG intensity does not automatically signify stronger net ferroelectric polarization when probing thin ferroelectric films. Rather, the relationship between \mathcal{R}_i and net \mathbf{P} depends on polarization configuration and wavelength of the SHG probe, and the direction of \mathbf{P} . When multiple $\chi^{(2)}$ tensor components contribute to \mathcal{R}_i , their relative phases, Fresnel factors, and spectra must also be taken into account. RA-SHG measurements for all four polarization configurations show similar intensities (see Supplemental Material [46]), indicating that

the relative phases between components are nonzero. These phase differences could be extracted via an interference-based SHG measurement between the SH field generated from the α - In_2Se_3 films and a reference source at the same wavelength. Quantitative understanding of the relationship between ferroelectric \mathbf{P} and SHG intensity thus requires the full spectroscopic analysis presented here.

V. CONCLUSION

We carried out a comprehensive suite of spectroscopic measurements of the linear and second-order nonlinear optical properties of vapor-deposited α - In_2Se_3 films as thin as 1 QL and as thick as bulk material. We then carried out *ab initio* calculations to link thickness-dependent optical properties quantitatively to crystalline and electronic structure. Energy minimization alone identified 2 energetically degenerate single-QL structures based on zincblende (ZB) or wurtzite (WZ) units, and 6 nearly degenerate 2-QL stacking configurations, for a total of 12 candidate 2-QL structures. We then carried out G_0W_0 calculations of the self-corrected band gap values, coupled with DFT-LDA calculations of the dielectric function $\epsilon(\omega)$ for 1 QL to bulk, and of all components of $\chi^{(2)}$ for 1 QL and for each of the 12 candidate 2-QL structures. After quasiparticle corrections, calculated band gaps and linear dielectric functions for 1 QL to bulk agreed well with both present and past measurements, but did not discriminate among the 12 candidate 2-QL configurations, all of which yielded similar calculated linear optical properties. Comparison of calculated and measured SHG, on the other hand, effectively discriminated among them. Single-wavelength, rotational-anisotropic (RA) SHG, by confirming $R3m$ symmetry of 2 QL layers, ruled out half of the candidate stacking configurations. SHG spectra then strongly supported the “down-up (DU)” stacking configuration, i.e., 2 QLs of WZ structure with opposing, outward-pointing electric polarizations.

This work has also demonstrated three important ways in which SHG complements conventional linear spectroscopy in characterizing thin ferroelectric films. First, SHG proved uniquely sensitive to relative rotations of individual QLs away from their minimum energy orientations, a feature that can be useful in characterizing moiré superlattices [82]. Second, SHG scanning microscopy yielded much higher-contrast images of single QLs than conventional white-light microscopy, by taking advantage of the contrast between the film's noncentrosymmetry and the mica substrate's centrosymmetry. Third, SHG is uniquely sensitive to ferroelectric polarization \mathbf{P} in layers as thin as 1 QL. This relationship is not, however, a simple proportionality between SHG intensity and net \mathbf{P} , but rather a subtle relationship that depends on the polarization and wavelength of the SHG probe, and the orientation and internal structure of the polarization.

Lastly, the present experimental and theoretical study of the optical spectra of α - In_2Se_3 could also be applied to many other ultrathin 2D materials; it has numerous applications and advantages: (1) SHG spectroscopy is a noninvasive optical probe capable of elucidating important structural features of ferroelectric materials [33] without having to add electrodes, disturbing the material, or needing to design and fabricate complex opto-electronic testing devices. (2) The theoretical

SHG spectra provides insight into electronic and atomic structure that are not available from other methods (for example, TEM), and can predict which structural variation or polytype is predominant in the synthesized samples. (3) The application of well-established *ab initio* theoretical methods such as DFT-LDA, TDDFT, and G_0W_0 can have considerable synergy with experiment, particularly when both intrinsic [$\epsilon(\omega)$, $\chi(2\omega)$] and extrinsic (transmission, SHG radiation) properties can be calculated.

ACKNOWLEDGMENTS

This work was supported by Robert Welch Foundation Grant No. F-1038 and CONACYT-Mexico research Project

No. A1-S-9410. Y. Cho acknowledges InProTUC (International Promovieren an der Technischen Universität Chemnitz) program for supporting her research at TU Chemnitz. Sample preparation was supported by Welch Foundation Grant No. F-1814, and the U.S. Department of Energy (DOE), Office of Science, Basic Energy Sciences, under Awards No. DE-SC0010308 and No. DE-SC0019025. Additionally, the authors thankfully acknowledge the computer resources, technical expertise, and support provided by the Laboratorio Nacional de Supercómputo del Sureste de México, a member of the CONACYT network of national laboratories as well as the Shared Hierarchical Academic Research Computing Network (SHARCNET) of Ontario, Canada.

-
- [1] Z. Yang and J. Hao, *Adv. Mater. Technol.* **4**, 1900108 (2019).
- [2] Z. Guan, H. Hu, X. Shen, P. Xiang, N. Zhong, J. Chu, and C. Duan, *Adv. Electron. Mater.* **6**, 1900818 (2020).
- [3] D. Boukhvalov, B. Gürbulak, S. Duman, L. Wang, A. Politano, L. Caputi, G. Chiarello, and A. Cupolillo, *Nanomaterials* **7**, 372 (2017).
- [4] S. Demirci, N. Avazlı, E. Durgun, and S. Cahangirov, *Phys. Rev. B* **95**, 115409 (2017).
- [5] J. Lin, Z. Fang, H. Tao, Y. Li, X. Huang, K. Ding, S. Huang, and Y. Zhang, *CrystEngComm* **20**, 2573 (2018).
- [6] H. Henck, D. Pierucci, J. Zribi, F. Bisti, E. Papalazarou, J.-C. Girard, J. Chaste, F. Bertran, P. Le Fèvre, F. Sirotti, L. Perfetti, C. Giorgetti, A. Shukla, J. E. Rault, and A. Ouerghi, *Phys. Rev. Mater.* **3**, 034004 (2019).
- [7] J.-S. Rhyee, K. H. Lee, S. M. Lee, E. Cho, S. I. Kim, E. Lee, Y. S. Kwon, J. H. Shim, and G. Kotliar, *Nature (London)* **459**, 965 (2009).
- [8] G. Han, Z.-G. Chen, C. Sun, L. Yang, L. Cheng, Z. Li, W. Lu, Z. M. Gibbs, G. J. Snyder, K. Jack, J. Drennan, and J. Zou, *CrystEngComm* **16**, 393 (2014).
- [9] L. Debbichi, O. Eriksson, and S. Lebègue, *Ann. Phys.* **526**, 402 (2014).
- [10] D. A. Bandurina, A. V. Tyurnina, G. L. Yu, A. Mishchenko, V. Zólyomi, S. V. Morozov, R. K. Kumar, R. V. Gorbachev, Z. R. Kudrynskiy, S. Pezzini, Z. D. Kovalyuk, U. Zeitler, K. S. Novoselov, A. Patané, L. Eaves, I. V. Grigorieva, V. I. Fal'ko, A. K. Geim, and Y. Cao, *Nat. Nanotechnol.* **12**, 223 (2016).
- [11] G. Liu, K. Chen, and J. Li, *J. Am. Ceram. Soc.* **101**, 36 (2018).
- [12] S. Wan, Y. Li, W. Li, X. Mao, C. Wang, C. Chen, J. Dong, A. Nie, J. Xiang, Z. Liu, W. Zhu, and H. Zeng, *Adv. Funct. Mater.* **29**, 1808606 (2019).
- [13] W. Li, F. P. Sabino, F. Crasto de Lima, T. Wang, R. H. Miwa, and A. Janotti, *Phys. Rev. B* **98**, 165134 (2018).
- [14] J. Quereda, R. Biele, G. Rubio-Bollinger, N. Agraït, R. D'Agosta, and A. Castellanos-Gomez, *Adv. Opt. Mater.* **4**, 1939 (2016).
- [15] D. Wu, A. J. Pak, Y. Liu, Y. Zhou, X. Wu, Y. Zhu, M. Lin, Y. Han, Y. Ren, H. Peng, Y.-H. Tsai, G. S. Hwang, and K. Lai, *Nano Lett.* **15**, 8136 (2015).
- [16] L. Hu and X. Huang, *RSC Adv.* **7**, 55034 (2017).
- [17] X. Tao and Y. Gu, *Nano Lett.* **13**, 3501 (2013).
- [18] B. Yu, S. Ju, X. Sun, G. Ng, T. D. Nguyen, M. Meyyappan, and D. B. Janes, *Appl. Phys. Lett.* **91**, 133119 (2007).
- [19] M. S. Choi, B. Cheong, C. H. Ra, S. Lee, J.-H. Bae, S. Lee, G.-D. Lee, C.-W. Yang, J. Hone, and W. J. Yoo, *Adv. Mater.* **29**, 1703568 (2017).
- [20] W. Ding, J. Zhu, Z. Wang, Y. Gao, D. Xiao, Y. Gu, Z. Zhang, and W. Zhu, *Nat. Commun.* **8**, 14956 (2017).
- [21] S. N. Shirodkar and U. V. Waghmare, *Phys. Rev. Lett.* **112**, 157601 (2014).
- [22] K. Chang, J. Liu, H. Lin, N. Wang, K. Zhao, A. Zhang, F. Jin, Y. Zhong, X. Hu, W. Duan, Q. Zhang, L. Fu, Q.-K. Xue, X. Chen, and S.-H. Ji, *Science* **353**, 274 (2016).
- [23] M. Wu and X. C. Zeng, *Nano Lett.* **16**, 3236 (2016).
- [24] D. D. Fong, G. B. Stephenson, S. K. Streiffer, J. A. Eastman, O. Auciello, P. H. Fuoss, and C. Thompson, *Science* **304**, 1650 (2004).
- [25] B. Meyer and D. Vanderbilt, *Phys. Rev. B* **63**, 205426 (2001).
- [26] M.-G. Han, M. S. J. Marshall, L. Wu, M. A. Schofield, T. Aoki, R. Twisten, J. Hoffman, F. J. Walker, C. H. Ahn, and Y. Zhu, *Nat. Commun.* **5**, 4693 (2014).
- [27] M. Dawber, K. M. Rabe, and J. F. Scott, *Rev. Mod. Phys.* **77**, 1083 (2005).
- [28] J. F. Scott, *Science* **315**, 954 (2007).
- [29] S. L. Miller and P. J. McWhorter, *J. Appl. Phys.* **72**, 5999 (1992).
- [30] B. H. Park, B. S. Kang, S. D. Bu, T. W. Noh, J. Lee, and W. Jo, *Nature (London)* **401**, 682 (1999).
- [31] S. Wan, Y. Li, W. Li, X. Mao, W. Zhu, and H. Zeng, *Nanoscale* **10**, 14885 (2018).
- [32] P. Ponath, K. Fredrickson, A. B. Posadas, Y. Ren, X. Wu, R. K. Vasudevan, M. B. Okatan, S. Jesse, T. Aoki, M. R. McCartney, D. J. Smith, S. V. Kalinin, K. Lai, and A. A. Demkov, *Nat. Commun.* **6**, 6067 (2015).
- [33] Y. Cho, P. Ponath, L. Zheng, B. Hatanpaa, K. Lai, A. A. Demkov, and M. C. Downer, *Appl. Phys. Lett.* **112**, 162901 (2018).
- [34] Y. Zhou, D. Wu, Y. Zhu, Y. Cho, Q. He, X. Yang, K. Herrera, Z. Chu, Y. Han, M. C. Downer, H. Peng, and K. Lai, *Nano Lett.* **17**, 5508 (2017).
- [35] J. Xiao, H. Zhu, Y. Wang, W. Feng, Y. Hu, A. Dasgupta, Y. Han, Y. Wang, D. A. Muller, L. W. Martin, P. A. Hu, and X. Zhang, *Phys. Rev. Lett.* **120**, 227601 (2018).
- [36] F. Xue, W. Hu, K.-C. Lee, L.-S. Lu, J. Zhang, H.-L. Tang, A. Han, W.-T. Hsu, S. Tu, W.-H. Chang, C.-H. Lien, J.-H. He,

- Z. Zhang, L.-J. Li, and X. Zhang, *Adv. Funct. Mater.* **28**, 1803738 (2018).
- [37] C. Zheng, L. Yu, L. Zhu, J. L. Collins, D. Kim, Y. Lou, C. Xu, M. Li, Z. Wei, Y. Zhang, M. T. Edmonds, S. Li, J. Seidel, Y. Zhu, J. Z. Liu, W.-X. Tang, and M. S. Fuhrer, *Sci. Adv.* **4**, eaar7720 (2018).
- [38] K. J. Kormondy, Y. Cho, A. B. Posadas, L. Zheng, K. Lai, Q. Wang, M. J. Kim, Q. He, A. Y. Borisevich, M. C. Downer, and A. A. Demkov, *Appl. Phys. Lett.* **113**, 132902 (2018).
- [39] C. Attaccalite, M. Palummo, E. Cannuccia, and M. Grüning, *Phys. Rev. Mater.* **3**, 074003 (2019).
- [40] L. Hu, X. Huang, and D. Wei, *Phys. Chem. Chem. Phys.* **19**, 11131 (2017).
- [41] X. Zhou, J. Cheng, Y. Zhou, T. Cao, H. Hong, Z. Liao, S. Wu, H. Peng, K. Liu, and D. Yu, *J. Am. Chem. Soc.* **137**, 7994 (2015).
- [42] J. Zhou, J. Shi, Q. Zeng, Y. Chen, L. Niu, F. Liu, T. Yu, K. Suenaga, X. Liu, J. Lin, and Z. Liu, *2D Mater.* **5**, 025019 (2018).
- [43] N. Leisgang, J. G. Roch, G. Froehlicher, M. Hamer, D. Terry, R. Gorbachev, and R. J. Warburton, *AIP Adv.* **8**, 105120 (2018).
- [44] M. Lin, D. Wu, Y. Zhou, W. Huang, W. Jiang, W. Zheng, S. Zhao, C. Jin, Y. Guo, H. Peng, and Z. Liu, *J. Am. Chem. Soc.* **135**, 13274 (2013).
- [45] W. Zheng, T. Xie, Y. Zhou, Y. L. Chen, W. Jiang, S. Zhao, J. Wu, Y. Jing, Y. Wu, G. Chen, Y. Guo, J. Yin, S. Huang, H. Q. Xu, Z. Liu, and H. Peng, *Nat. Commun.* **6**, 6972 (2015).
- [46] See Supplemental Material at <http://link.aps.org/supplemental/10.1103/PhysRevMaterials.6.034006> for more procedural details on the experiments and calculations presented in this work.
- [47] J. Zhou, Q. Zeng, D. Lv, L. Sun, L. Niu, W. Fu, F. Liu, Z. Shen, C. Jin, and Z. Liu, *Nano Lett.* **15**, 6400 (2015).
- [48] J. Ye, S. Soeda, Y. Nakamura, and O. Nittono, *Jpn. J. Appl. Phys.* **37**, 4264 (1998).
- [49] Y. Li, Y. Rao, K. F. Mak, Y. You, S. Wang, R. Dean, and T. F. Heinz, *Nano Lett.* **13**, 3329 (2013).
- [50] CompleteEASE software from J. A. Woollam, <https://www.jawoollam.com/ellipsometry-software/completeease>.
- [51] J. Tauc, R. Grigorovici, and A. Vancu, *Phys. Status Solidi B* **15**, 627 (1966).
- [52] J. Tauc, *Mater. Res. Bull.* **3**, 37 (1968).
- [53] J. Bloch, J. G. Mihaychuk, and H. M. van Driel, *Phys. Rev. Lett.* **77**, 920 (1996).
- [54] P. Giannozzi, O. Andreussi, T. Brumme, O. Bunau, M. Buongiorno Nardelli, M. Calandra, R. Car, C. Cavazzoni, D. Ceresoli, M. Cococcioni, N. Colonna, I. Carnimeo, A. Dal Corso, S. de Gironcoli, P. Delugas, R. A. DiStasio, A. Ferretti, A. Floris, G. Fratesi, G. Fugallo *et al.*, *J. Phys.: Condens. Matter* **29**, 465901 (2017).
- [55] L. Hedin, *Phys. Rev.* **139**, A796 (1965).
- [56] X. Gonze, B. Amadon, G. Antonius, F. Arnardi, L. Baguet, J.-M. Beuken, J. Bieder, F. Bottin, J. Bouchet, E. Bousquet, N. Brouwer, F. Bruneval, G. Brunin, T. Cavignac, J.-B. Charraud, W. Chen, M. Côté, S. Cottenier, J. Denier, G. Geneste *et al.*, *Comput. Phys. Commun.* **248**, 107042 (2020).
- [57] A. H. Romero, D. C. Allan, B. Amadon, G. Antonius, T. Applencourt, L. Baguet, J. Bieder, F. Bottin, J. Bouchet, E. Bousquet, F. Bruneval, G. Brunin, D. Caliste, M. Côté, J. Denier, C. Dreyer, P. Ghosez, M. Giantomassi, Y. Gillet, O. Gingras *et al.*, *J. Chem. Phys.* **152**, 124102 (2020).
- [58] X. Gonze, B. Amadon, P.-M. Anglade, J.-M. Beuken, F. Bottin, P. Boulanger, F. Bruneval, D. Caliste, R. Caracas, M. Côté, T. Deutsch, L. Genovese, P. Ghosez, M. Giantomassi, S. Goedecker, D. R. Hamann, P. Hermet, F. Jollet, G. Jomard, S. Leroux *et al.*, *Comput. Phys. Commun.* **180**, 2582 (2009).
- [59] N. Troullier and J. L. Martins, *Phys. Rev. B* **43**, 1993 (1991).
- [60] V. Olevano, L. Reining, and F. Sottile, <http://dp-code.org>.
- [61] L. Reining, V. Olevano, F. Sottile, S. Albrecht, and G. Onida, <http://www.bethe-salpeter.org>.
- [62] B. S. Mendoza, F. Nastos, N. Arzate, and J. E. Sipe, *Phys. Rev. B* **74**, 075318 (2006).
- [63] B. S. Mendoza, S. M. Anderson, J. L. Cabellos, and T. Rangel, TINIBA: *Ab initio* calculation of the optical properties of solids, surfaces, interfaces, and 2D materials, INDAUTOR-Mexico No. 03-2009-120114033400-01.
- [64] S. M. Anderson, N. Tancogne-Dejean, B. S. Mendoza, and V. Vénier, *Phys. Rev. B* **91**, 075302 (2015).
- [65] N. Tancogne-Dejean, C. Giorgetti, and V. Vénier, *Phys. Rev. B* **92**, 245308 (2015).
- [66] S. M. Anderson and B. S. Mendoza, *J. Open Source Software* **2**, 242 (2017).
- [67] S. M. Anderson and B. S. Mendoza, *Phys. Rev. B* **94**, 115314 (2016).
- [68] S. M. Anderson, Y. Cho, and B. S. Mendoza, [arXiv:1712.04991](https://arxiv.org/abs/1712.04991).
- [69] J. I. Dadap, Z. Xu, X. F. Hu, M. C. Downer, N. M. Russell, J. G. Ekerdt, and O. A. Aktsipetrov, *Phys. Rev. B* **56**, 13367 (1997).
- [70] S. M. Anderson, N. Tancogne-Dejean, B. S. Mendoza, and V. Vénier, *Phys. Rev. B* **93**, 235304 (2016).
- [71] A. Chaiken, K. Nauka, G. A. Gibson, H. Lee, C. C. Yang, J. Wu, J. W. Ager, K. M. Yu, and W. Walukiewicz, *J. Appl. Phys.* **94**, 2390 (2003).
- [72] L. Debbichi, O. Eriksson, and S. Lebégue, *J. Phys. Chem. Lett.* **6**, 3098 (2015).
- [73] M. Eddrief, C. Julien, M. Balkanski, and K. Kambas, *Mater. Lett.* **2**, 432 (1984).
- [74] C.-H. Ho, C.-H. Lin, Y.-P. Wang, Y.-C. Chen, S.-H. Chen, and Y.-S. Huang, *ACS Appl. Mater. Interfaces* **5**, 2269 (2013).
- [75] M. Ishikawa and T. Nakayama, *Jpn. J. Appl. Phys.* **36**, L1576 (1997).
- [76] R. B. Jacobs-Gedrim, M. Shanmugam, N. Jain, C. A. Durcan, M. T. Murphy, T. M. Murray, R. J. Matyi, R. L. Moore, and B. Yu, *ACS Nano* **8**, 514 (2014).
- [77] C. Julien, M. Eddrief, K. Kambas, and M. Balkanski, *Thin Solid Films* **137**, 27 (1986).
- [78] N. Narita, S. Nagai, S. Saito, and K. Nakao, *J. Phys. Soc. Jpn.* **60**, 1279 (1991).
- [79] Z. Q. Zheng, J. D. Yao, and G. W. Yang, *J. Mater. Chem. C* **4**, 8094 (2016).
- [80] R. Minnings, A. I. Shkrebtii, G. Perinparajah, N. Arzate, S. Anderson, B. Mendoza, Y. Cho, M. Downer, and D. Zahn, in *37th European Photovoltaic Solar Energy Conference and Exhibition* (Curran Associates, Red Hook, NY, 2020), pp. 51–55.
- [81] T. R. Bader and A. Gold, *Phys. Rev.* **171**, 997 (1968).
- [82] K. Yao, N. R. Finney, J. Zhang, S. L. Moore, L. Xian, N. Tancogne-Dejean, F. Liu, J. Ardelean, X. Xu, D. Halbertal, K. Watanabe, T. Taniguchi, H. Ochoa, A. Asenjo-Garcia, X. Zhu, D. N. Basov, A. Rubio, C. R. Dean, J. Hone, and P. J. Schuck, *Sci. Adv.* **7**, eabe8691 (2021).